Application of Signal Imaging Analysis Technology in Prediction and Treatment of Water Inrush in Diversion Tunnel

Jun Yao[1,2], Yuan Wang[1*], Di Feng[1]

[1] College of Civil and Transportation Engineering, Hohai University, Nanjing 210098, China
[2] College of Urban Construction and Transportation, Hefei University, Hefei 230601, China

Corresponding Author Email: wangyuan@hhu.edu.cn

ABSTRACT

A signal imaging analysis technology was proposed to accurately interpret geological radar detection images in order to address the issues of difficult interpretation of radar advance forecast images of water inrush in diversion tunnels in unfavorable geological zones and difficult detection of grouting effects in grouting circles. The waveform, amplitude, and frequency differences in the radar data among various geological bodies in the fracture development zone, broken zone, and water-rich zone can be analyzed by the signal imaging analysis technology, which can extract multiple technical parameters for comprehensive judgment and provide a foundation for the interpretation of geological radar images. In this study, signal mapping analysis technology was used to interpret the geological detection images taken in front of the tunnel face and the surrounding rock geological detection map after cement-polyvinyl alcohol grouting, respectively. The accuracy of the signal mapping analysis technology was confirmed, and the following conclusions were drawn: (1) Geographic Different geological structures, such as fissure zones, broken zones, and water-rich zones, have different reflection signal properties for radar electromagnetic waves. With the help of the image, distinct geological features can be identified and water inrush can be anticipated; (2) Electronic scanning imaging can be used to observe it. The geological radar image feedback of the grouting circle after grouting indicates that the lithology of the grouting circle is complete and the grouting reinforcement and sealing effect is good when the cement-polyvinyl alcohol slurry concretion particles are dense; (3) The numerical analysis results of the seepage field of the tunnel demonstrate that the grouting of the surrounding rock can effectively reduce water seepage and control water gushing. The study's findings offer a specific reference point for the forecasting and management of water gushing in diversion tunnels located in adverse geological regions.

1. INTRODUCTION

The tunnel water gushing problem is a significant engineering construction disaster problem when the water diversion tunnel project is excavated in unfavorable geology such as karst zone, fractured zone, and water-rich zone. When the water gushes, a significant volume of groundwater pours into the tunnel, resulting in issues like tunnel instability, a reduction in groundwater levels, ground subsidence, and the drying out of surface flora, as well as significant financial losses and environmental harm. Therefore, it is crucial to research tunnel water inrush forecasting technologies as well as inrush management strategies.

Researchers domestically and internationally have studied advance prediction technology for tunnel water gushing and surrounding rock grouting reinforcement technology in order to prevent and control tunnel water gushing. Liu et al. [1] proposed an HGWO-SVR tunnel water inrush prediction model using the Hybrid Gray Wolf Optimization (HGWO) algorithm and the Support Vector Regression (SVR) technique. High precision and fewer samples are needed with the prediction model. In order to classify different types of groundwater and create hydrogeological models for tunnel sites, Kang et al. [2] used the fuzzy data analysis method to

examine the content of common ions in gushing water. A static-dynamic water inrush risk assessment method was put forth by Song et al. [3] in 2021. A dynamic water inrush risk prediction approach was developed by fusing the static evaluation model and the advanced prediction method. Prediction offers a solid theoretical foundation. In order to accurately estimate the scope and geographic location of the linked catastrophic source of water and mud inrush in Shangjiawan strong karst tunnel, Yuan [4] developed a thorough advanced prediction method in conjunction with advanced drilling. Through several field testing, modeling experiments, FDTD numerical simulation, and real-world engineering applications, Cao et al. [5], summarized the radar-based reservoir leakage analysis approach. The location and direction of reservoir leakage can be accurately determined using this method, supplying technical assistance for reservoir reinforcement project design and construction. In order to successfully apply his multi-point thermal sensor technology in engineering, Radzicki et al. [6] created active (heated) thermal methods for leak detection and in-situ measurement of seepage velocity. Geological radar imaging is a challenge to interpret, but Liu et al. [7] introduced an improved back-projection imaging technique that can bring the reflected wave closer to the actual geological border with less fake clutter. A

mobile power source technique (MESM) with high precision for water-bearing exploration and compliance with the requirements for advanced geological tunnel investigation was proposed by Guo et al. [8]. Through laboratory testing, Peng et al. [9] examined the effects of water glass content, Baume degree, and powder-material ratio on the functionality of the slurry. High compressive strength, controlled setting time, and environmental protection are its benefits. In slurry work, it works best. Zhang et al. [10] proposed an organic combination of sodium silicate, cement, polyethylene glycol (PEG) 200, hydrogen double bond polymerization, and polycarboxylate-based superplasticizer with excellent synergistic interaction with inorganic hybrid chemical grouting material. The findings demonstrate that C-S-P has superior mechanical properties and grouting performance, both of which are necessary for the quick excavation of tunnels filled with loose sediment. Many academics have proposed techniques for grouting reinforcement for nearby rocks and used predictive models, evaluation methods, radar forecasting, and other techniques to predict water inrush.

There is not much research, nevertheless, on how to interpret radar detection images and how signals affect imaging features. This study examines the effects of variations in phase, amplitude, and frequency in reflected waves on imaging and highlights the features of normal geological imaging. It begins with the detection mechanism of ground radar and employs signal imaging analysis technology to explore these effects [11]. Give a theoretical foundation for predicting tunnel water inrush. Additionally, the grouting reinforcing impact of the surrounding rock is detected using the signal imaging technology, and this is confirmed by numerical analysis, demonstrating the dependability of the geological radar signal imaging technology [12].

2. IMAGING TECHNIQUE OF GPR DETECTION TECHNOLOGY

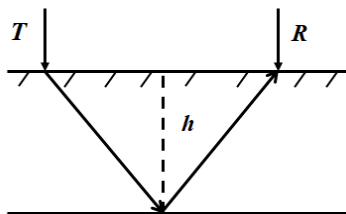### 2.1 Principle of GPR detection technology

Figure 1. Schematic diagram of ground radar detection

Geological radar is a device that detects the distribution or shape of materials inside a medium using high-frequency electromagnetic waves. Geomagnetic wave receivers and electromagnetic wave transmitters make up its primary parts. According to the equipment system, the electromagnetic wave transmitting device transmits high-frequency broadband pulsed electromagnetic waves (10MHz–1GHz) to the detection medium, and the receiving device receives electromagnetic waves reflected from the detection medium. By processing the radar signal data, the receiving device then creates a map using the detected electromagnetic waves, as shown in Figure 1. After the electromagnetic wave is launched, it will be reflected by various rock mass interfaces in the detecting medium due to the electrical differences between the

different media [13]. The reflected wave has significant variations in its amplitude, frequency, wave velocity, phase, and other properties due to the varied electrical and geometric features of the materials inside the detecting medium. Therefore, based on the reflected electromagnetic wave waveform, strength, round-trip time, and other data, the system will evaluate the actual geological state in the detecting medium [14, 15].

2.2 Signal imaging analysis

The reflected real signal received by the geomagnetic wave receiving device can be expressed as:

$$f(t) = A(t)\cos[\omega_0 t + \varphi(t)] \tag{1}$$

where, $A(t)$ is the amplitude function; t is time; ω_0 is the central frequency; $\varphi(t)$ is the phase function.

Eq. (1) demonstrates how variables like waveform amplitude, frequency, and phase are all reflected in one reflected signal. This makes it challenging to feed back the varying features of various parameters in various geologies, which has an impact on image interpretation. The signal data is broken down into instantaneous amplitude, instantaneous frequency, and instantaneous phase, and the signal data is interpreted through many parameters in order to accurately assess the imaging maps of signals in various geologies.

A Hilbert transform is needed to examine the reflected wave properties. Assume that the input signal is $f(t)$, the Hilbert frequency response $H(\omega)$ filters it to produce an output signal $\overline{f}(t)$, and the Hilbert formula is:

$$\overline{f}(t) = f(t)\frac{1}{\pi t} \tag{2}$$

$$g(t) = f(t) + i\overline{f}(t) = f(t) + if(t)\frac{1}{\pi t} \tag{3}$$

Substituting (1) into (3):

$$g(t) = A(t)\{\cos[\omega_0 t + \varphi(t)] + i\sin[\omega_0 t + \varphi(t)]\} \tag{4}$$

where, $A(t)$ is the amplitude function of the reflected wave, that is, the instantaneous amplitude. The instantaneous amplitude can be derived from formulas (3) and (4):

$$A(t) = \sqrt{g^2(t) + \overline{g}^2(t)} \tag{5}$$

The instantaneous phase $\theta(t) = \omega_0 t + \varphi(t)$ of the reflected wave can be obtained from Eqns. (3) and (4):

$$\theta(t) = \arctan[\frac{\overline{g}(t)}{g(t)}] \tag{6}$$

The derivative of the phase to time is the instantaneous frequency of the reflected wave, and the instantaneous frequency can be deduced from formula (6):

$$S(t) = \frac{d\theta(t)}{dt} = \frac{d}{dt}\arctan[\frac{\overline{g}(t)}{g(t)}] \tag{7}$$

The instantaneous phase is unaffected by the signal strength and can reflect the continuity of the event axis; the instantaneous amplitude reflects the change law of the reflected wave energy due to encountering different media; and the instantaneous frequency reflects the time change rate of the phase, when the lithology changes, the reflected wave. Rock stability can be determined using the frequency, which is subject to large change.

2.3 Analysis of typical geological imaging features

Water gushing primarily occurs in water-rich zones, joint fissure development zones, and fault fracture zones in diversion tunnels. Signal imaging technology is used to analyze the traits of typical unfavorable geological radar imaging images to provide a reference for image interpretation in order to carry out advanced water inrush prediction.

The porosity and water content of the rock in the shattered zone are rather high, and compared to the intact rock, its reflection coefficient and dielectric constant are very different. The electromagnetic wave is reflected at the fault and fracture interface as it travels through the whole rock and enters the shattered zone. The waveform is chaotic, the high-frequency part attenuates quickly, the automatic gain gradient is large, the energy of the reflected wave increases, the amplitude increases quickly, and diffraction and scattering frequently occur in the broken zone and fissure zone.

The dielectric constant of the water, which accumulates in the water-rich zone, is substantially greater than that of the rock. Between the two, there is a substantial electrical difference. The electromagnetic wave creates strong reflections when it hits the water-rich zone's interface and multiple strong reflections in a specific order as it goes through the water layer; frequency Significantly lowered, period lengthened; the reflected wave waveform is homogenous and less influenced by the continuous water surface distribution.

The difference between bedrock and radar imaging is obvious because fracture-intensive zones are primarily distributed in fault zones and weak interlayers, and there are fillers with various components inside, which results in electrical differences with the surrounding bedrock. The waveform is chaotic and irregular when passing through the crack zone, indicating that the filling in the fracture is not uniform. Strong interface reflection waves are generated when the electromagnetic wave enters the crack interface, and the continuity of the event reflects the roughness of the crack.

The mapping characteristics of the broken zone, joint fissure zone, and water-rich zone can be clearly distinguished on the geological radar map through the use of signal imaging analysis technology, which offers a strong assurance for the advanced prediction of water inrush [16].

2.4 Application case analysis

Water from Chun'an County of Qiandao Lake is pumped through the Hangzhou Qiandao Lake Diversion Tunnel and diverted to Xianlin Reservoir in Hangzhou. The gravity flow of water is delivered through pressure tunnels along the 123.34km long water delivery line. Complex geological conditions can be found in the area. The lithology of the surrounding rock is primarily quartz sandstone, the grade of the rock is grade IV, the joints and fissures are highly developed, the weathering along the fissure surface is strong,

and there is fissure water at the k4+410 tunnel face upstream of the Shimaofan main cave. For precise detection 30 meters in front of the tunnel, the SL-GPR wireless ground-penetrating radar is used. Figure 2 depicts the survey line's layout, while Figures 3 and 4 depict the detecting radar's imaging images.
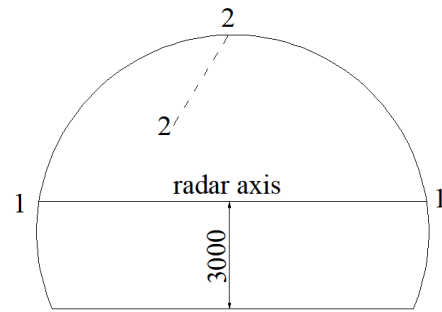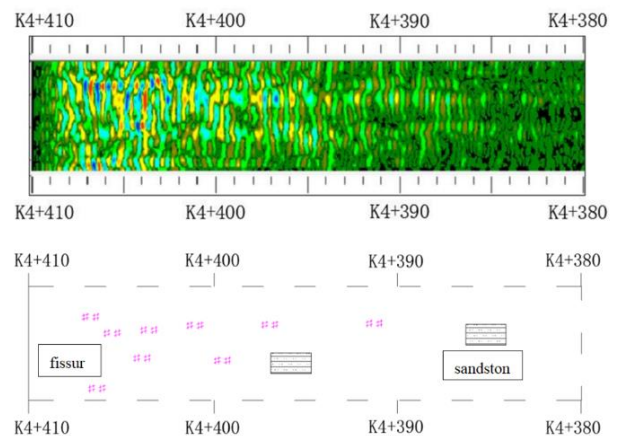

Figure 2. Distribution map of radar survey lines
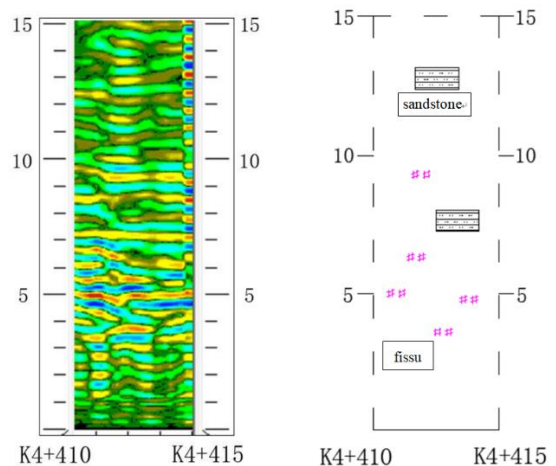

Figure 3. 1-1 positioning line radar image

Figure 4. 2-2 positioning line radar image

This time, the radar detection pile number K4+410K4+380, the localized strength of the radar reflection wave in the section, the predominant frequency being medium and low frequency, and the localized low area. It is assumed that the quartz sandstone dominates the lithology in the detection range and that the rock mass generally bad, but the pile number K4+412K4+400 section's reflected wave amplitude around the face's center is very strong, the frequency is low, and the phase axis continuity is particularly bad as a groundwater resource.

The energy of the reflected wave is regionally strong within the vault's 15 m depth range, the frequency is dominated by the intermediate frequency, the local is low, and the continuity of the same phase is subpar, reflecting hollow magnetic abnormality.

Geological radar technology uses signal processing to create an image after detecting the face's geological condition. A useful reference for water gushing forecast, the image information depicts the interior cracks, shattered zones, water, and other information of the rock mass. gave a resounding assurance.

3. GROUTING EFFECT OF CEMENT-POLYVINYL ALCOHOL GROUT

The best way to prevent incidents with water gushing in tunnels with adverse geology is to inject grout into the surrounding rock, reinforce the rock to minimize its permeability, restrict the water outside the grouting circle, and ensure the safety of the tunnel lining. Although pure cement slurry has benefits such as a high calculus rate and good viscosity, etc., the water blocking performance is inadequate because to the lengthy setting period and numerous pores in the concretion body. Polyvinyl alcohol is combined with cement grout to speed up the process of setting the grout and increase the crack resistance of stones that have been grouted [17].

3.1 Setting time characteristics of cement-polyvinyl alcohol double slurry

PVA is a low-cost, high molecular-weight polymer with exceptional water solubility. After gelation and film production, the polyvinyl alcohol exhibits good deformation characteristics as well as good toughness. The PVA solution and cement liquid mix well together. When the two solutions are mixed, the gel creates a film with good plasticity, and the cement is shielded from corrosion by a film, increasing the stone body's resistance to cracking and durability.

Table 1. Gel time of double slurry with different concentrations and different water-cement ratios

W/C Concentration	0.5:1	0.75:1	1:1	1.5:1
1%	189	654	1108	1598
2%	174	612	1097	1574
3%	154	563	1006	1528
4%	121	487	987	1503
5%	97	425	945	1458

When heated to 80 degrees and stirred for 20 hours with a magnetic stirrer, polyvinyl alcohol is challenging to dissolve in water at room temperature. The concentration of polyethylene is 1%, 2%, 3%, 4%, and 5%. Alcohol aqueous solution, cement slurry volume, cement solution volume, and a mixture of PVA solutions at various concentrations When measuring the gel time of various concentrations of PVA solution and cement solution with various water-cement ratios to form double slurry using the inverted cup method, the precise results are shown in Table 1.

Table 1 shows that, under various water-cement ratios and polyvinyl alcohol concentrations, the gel time of cement-polyvinyl alcohol slurry is in the range of 97s-1458s, all within

half an hour, which essentially satisfies the criteria of grouting construction. necessary time for material to gel. The gel time decreases with increasing polyvinyl alcohol concentration under the same water-cement ratio and can be reduced by almost 50%, showing that the concentration of polyvinyl alcohol has a significant impact on the gel time. At the same concentration of polyvinyl alcohol, the water-cement ratio increases. The longer the value, which is consistent with the gel time of pure cement slurry, the longer the gel time.

3.2 Microscopic characteristics of cement-polyvinyl alcohol slurry stones

The cement slurry and cement-polyvinyl alcohol slurry stones were taken for scanning electron microscopy in order to verify the anti-cracking performance of the two slurry stones. The microscopic characteristics of the two slurry stones were then observed from a microscopic point of view. In Table 2, the grout's specifications are displayed.

Table 2. Preparation of slurry for scanning electron microscopy

No.	Slurry name	Water-cement ratio	Additive volume ratio	Admixture concentration	Age
A01	Cement slurry	1:1	/	/	3d
A02	Cement-polyvinyl alcohol	1:1	4:1	5%	3d

The test used a Hitachi SU8010 cold field emission scanning electron microscope, as seen in Figures 5 and 6. In order to conduct the test, samples were first taken from two different types of slurry stones and pasted on conductive tape. After that, the samples were placed in the vacuum treatment equipment, vacuumed, and then sprayed with gold. Finally, the samples were scanned under a microscope to look for microscopic cracks.


Figure 5. Cold field emission scanning electron microscope


Figure 6. Test block gold spraying equipment

As illustrated in Figure 7 (a), (b), the cement slurry concretions have a large number of pores that are dispersed randomly across the grout concretions. High water pressure will cause the pores to continue to grow, enlarge, and produce cracks. This will enhance the permeability of the grout stone body and have an impact on the grouting effect.

Figure 7 (c), (d) shows that the cement-polyvinyl alcohol slurry stone body is generally compact, free of pores and early cracks, and that the polyvinyl alcohol applied to its surface has an effect on the stone body's ability to resist cracking in order to meet the demands of the surrounding rock grouting under high water pressure.
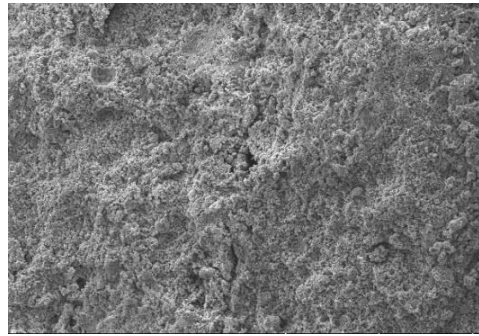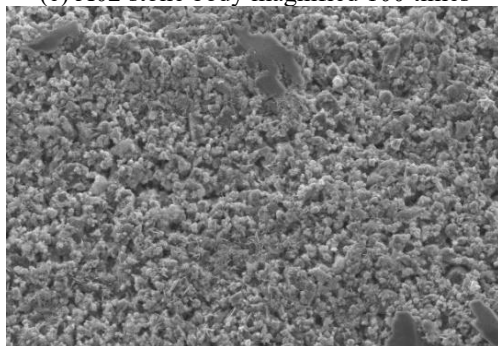

(a) A01 stone body magnified 100 times
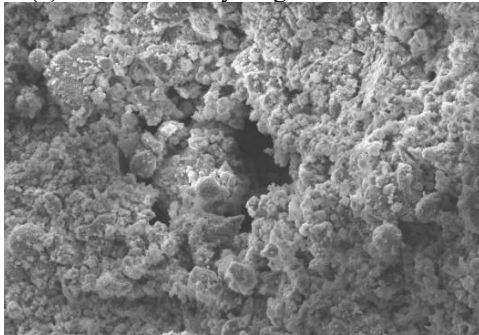
(b) A01 stone body magnified 500 times
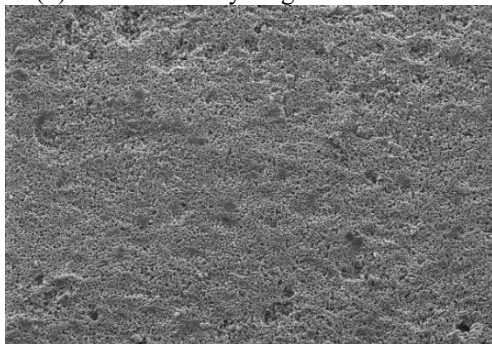
(c) A02 stone body magnified 100 times


(d) A02 stone body magnified 500 times

Figure 7. Electron microscopic scanning diagram of stone body

3.3 Radar imaging after grouting surrounding rock

According to the data above, cement-polyvinyl alcohol is the best grouting material for blocking water. It is challenging to see whether the grout after grouting has filled and consolidated the fissures and fractured areas in the surrounding rock, though. It is challenging to identify the slurry effect. Therefore, the same location line's Pearl River area was once more detected using geological radar, and the grouting effect was assessed by interpreting the detection map in accordance with signal imaging technology, as shown in Figure 8.
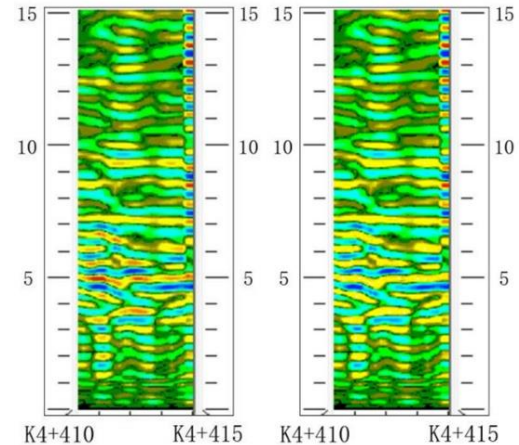
(a) 2-2 Comparison before and after lateral line grouting
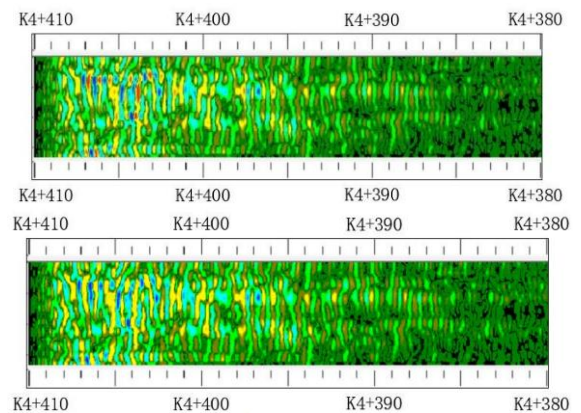
(b) 1-1 Comparison before and after lateral line grouting

Figure 8. Comparison of ground radar images before and after grouting

Figure 8 illustrates that the expected grouting effect is achieved and that the energy of the geological radar reflection wave in the grouting circle decays slowly, has a low amplitude, and has a relatively uniform waveform. This indicates that the overall quality of the rock mass is good.

4. GROUTING EFFECT ON WATER GUSHING CONTROL

The numerical calculation method is used to analyze the seepage field characteristics of the tunnel surrounding rock after grouting and to assess the grouting effect in order to confirm the effectiveness of tunnel grouting to control water gushing [18].

4.1 Model information

At k4+410 meters of Hangzhou Qiandao Lake Diversion Tunnel, the overlying rock formation is 327 meters, IV surrounding rock, the permeability coefficient of the surrounding rock is 1×10^{-5} m/s, and the permeability is strong; the groundwater level is 2 meters above the ground, and the water head at the center of the tunnel is 325 meters , the permeability coefficient of the grouting ring is a variable; the inner chamber of the cave is simplified as a circle, the equivalent inner diameter of the lining is 6.7 m, the equivalent outer diameter is 8.4 m, and the thickness of the lining is 0.85m.

To simulate the tunnel excavation and grouting operation, create a two-dimensional seepage-stress coupling model using the ABAQUS program. The influence range of 10 times the tunnel diameter is taken into account by the model. The design model is 84 meters wide and 130 meters high, with bottom and left- and right-side horizontal displacement constraints set. Vertical displacement constraints; the left and right boundaries are impermeable; the top of the model is impermeable; the inner surface of the lining is permeable; the water pressure is set to 0; the earth pressure coefficient is 0.9; and the pore water pressure is 2.25 on the top and 3.55 on the bottom of the model [19, 20].

Grouting into the surrounding rock through a certain grouting technology, the permeability coefficient of the surrounding rock decreases after grouting, and the permeability coefficient of the grouting circle is respectively taken as 1×10^{-5} m/s, 1×10^{-6} m/s, 1×10^{-7} m/s, and 1×10^{-8} m/s within the grouting range, and the numerical calculation is carried out.

4.2 Calculation result analysis

The cloud diagram of pore pressure distribution in seepage field is shown in Figure 9 under the four conditions of permeability coefficient of grouting circle.

From Figure 9, it can be found that the permeability of the grouting ring has a significant effect on the external water pressure of the lining, and the external water pressure of the lining decreases significantly with the decrease of the permeability coefficient of the grouting ring. When the permeability coefficient of the grouting ring is 1×10^{-5} m/s, that is, when there is no grouting, the water pressure outside the lining is the largest, reaching 2.24MPa; when the grouting of the surrounding rock begins, the permeability of the surrounding rock within the grouting range decreases, and the water outside the lining When the pressure is 1.35MPa, the external water pressure of the lining significantly decreases to only 60.3% without grouting; when k=1×10^{-7} m/s, it is already relatively small and is in a safe state; when k≤1×10^{-8} m/s, the external water pressure of the lining is very small, and it no longer decreases with the decrease of the permeability coefficient of the grouting circle, and is in a stable state, mainly because the permeability coefficient of the grouting circle is very small. Small and almost impermeable, most of the external water pressure is borne by the grouting ring. The above rules show that after grouting, the surrounding rock is in a state of low permeability, which can better control the water inrush disaster.
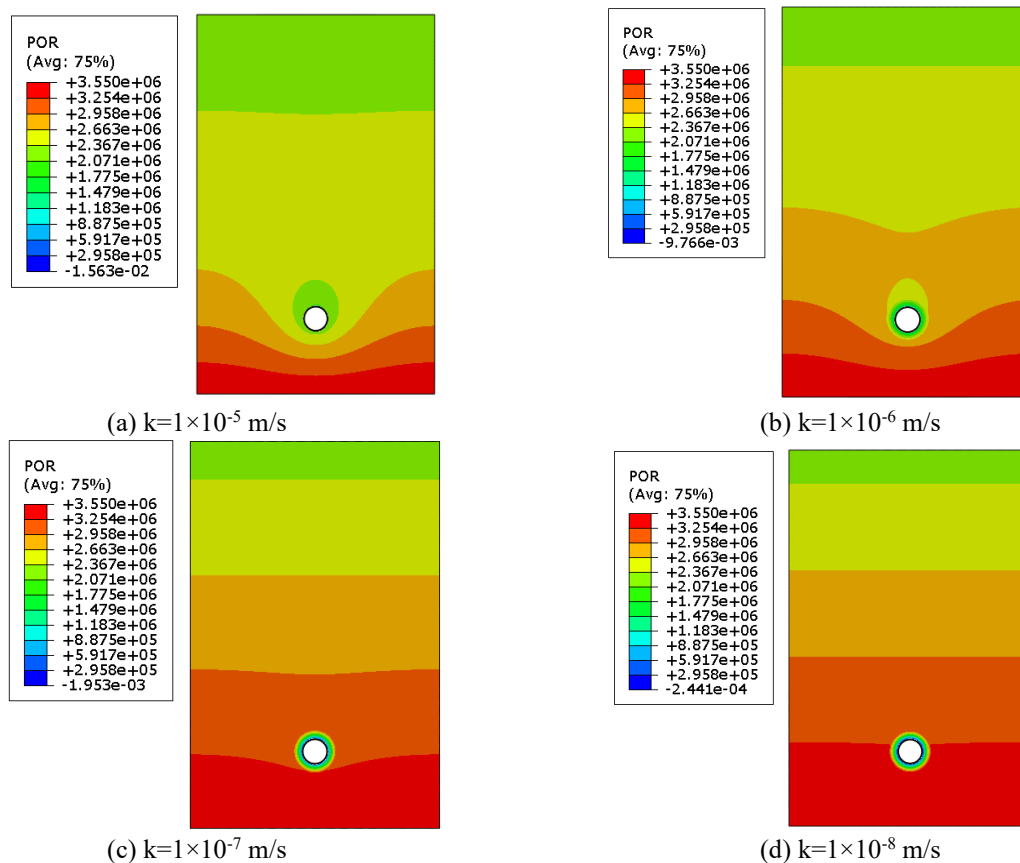

(a) k=1×10^{-5} m/s

(b) k=1×10^{-6} m/s

(c) k=1×10^{-7} m/s

(d) k=1×10^{-8} m/s

Figure 9. Influence of permeability coefficient of grouting circle on pore pressure of seepage field

5. CONCLUSIONS

The imaging analysis technology of a geological radar signal is the focus of this paper, which also examines its application to the detection of grouting circle effects after tunnel grouting reinforcement treatment and the prediction of tunnel water inrush. The paper comes to the following conclusions:

(1) Due to electrical differences, shape, size, and continuity differences in the detection medium, geological radar electromagnetic waves in the fissure zone, broken zone, and water-rich zone have obvious differences in the reflected wave waveform, amplitude, and frequency, and the system will reflect the signal. Geological radar technology has a good advanced forecasting function, and the data is converted into images that can reflect the precise geological distribution in front of the drill face;

(2) The cement-polyvinyl alcohol used for tunnel grouting has good quick-setting properties, and the particles are tightly packed and have low permeability. The energy of the geological radar reflection wave decays slowly, the amplitude is small, and the waveform is largely uniform following grouting in the surrounding rock, reflecting the general quality of the rock mass and achieving the anticipated goal of grouting treatment;

(3) The grouting circle can effectively reduce the amount of water seepage, and the cracks and fault zones in the surrounding rock are effectively blocked and reinforced, which is consistent with the geological radar, by numerically simulating the water blocking effect of tunnel grouting. The grouting material is cement-polyvinyl alcohol. The reliability of ground radar technology is demonstrated by the consistency of the reflected wave display effect.

REFERENCES

[1] Liu, D., Xu, Q., Tang, Y., Jian, Y. (2020). Prediction of water inrush in long-lasting shutdown karst tunnels based on the HGWO-SVR model. IEEE Access, 9: 6368-6378. https://doi.org/10.1109/ACCESS.2020.3047626

[2] Kang, X., Luo, S., Xu, M., Zhang, Q., Yang, Y. (2019). Dynamic estimating the karst tunnel water inrush based on monitoring data during excavation. Acta Carsologica, 48(1). https://doi.org/10.3986/ac.v48i1.4654

[3] Song, T., Zeng, J., Ma, J., Ma, C., Li, T., Xia, T. (2021). Water inrush risk assessment based on AHP and advance forecast approach: A case study in the micangshan tunnel. Advances in Civil Engineering, 2021. https://doi.org/10.1155/2021/9750447

[4] Yuan, Y. (2017). Comprehensive analysis on disaster associated by water inrush and mud gushing in Shangjiawan karst tunnel. Journal of Central South University, 48(1): 203-201. https://doi.org/10.11817/j.issn.1672-7207.2017.01.028

[5] Cao, J., Yuan, B., Bai, Y. (2021). Simulation study on image characteristics of typical GPR targets in water conservancy projects. Geofluids, 2021. https://doi.org/10.1155/2021/5550620

[6] Radzicki, K., Gołębiowski, T., Ćwiklik, M., Stoliński, M. (2021). A new levee control system based on geotechnical and geophysical surveys including active thermal sensing: A case study from Poland. Engineering Geology, 293: 106316. https://doi.org/10.1016/j.enggeo.2021.106316

[7] Liu, B., Zhang, F., Li, S., Li, Y., Xu, S., Nie, L., Zhang, Q. (2018). Forward modelling and imaging of ground-penetrating radar in tunnel ahead geological prospecting. Geophysical Prospecting, 66(4): 784-797. https://doi.org/ 10.1111/1365-2478.12613

[8] Guo, Q., Nie, L., Li, N., Yang, W., Lin, C., Liu, B., Shi, Y. (2019). Water-bearing body prospecting ahead of tunnel face using moving electrical-source method. Geotechnical and Geological Engineering, 37(3), 2047-2064. https://doi.org/10.1007/s10706-018-0743-0

[9] Peng, L., Yan, C., Sun, G., Xi, L., Liu, J. (2016). Experimental study on performance of grouting material for repairing surrounding rock in river intake tunnel. Geotechnical Investigation & Surveying.

[10] Zhang, C., Yang, J., Fu, J., Ou, X., Xie, Y., Liang, X. (2019). Performance evaluation of modified cement-sodium silicate grouting material for prereinforcing loose deposit tunnels. Journal of Materials in Civil Engineering, 31(7): 06019003. https://doi.org/10.1061/(ASCE)MT.1943-5533.0002747

[11] Hassani, A.N., Farhadian, H., Katibeh, H. (2018). A comparative study on evaluation of steady-state groundwater inflow into a circular shallow tunnel. Tunnelling and Underground Space Technology, 73: 15-25. https://doi.org/10.1016/j.tust.2017.11.019

[12] Barani, O.R., Khoei, A.R., Mofid, M. (2011). Modeling of cohesive crack growth in partially saturated porous media; a study on the permeability of cohesive fracture. International Journal of Fracture, 167(1): 15-31. https://doi.org/10.1016/j.engfracmech.2014.04.016

[13] Lunina, O.V., Denisenko, I.A. (2020). Single-event throws along the Delta Fault (Baikal rift) reconstructed from ground penetrating radar, geological and geomorphological data. Journal of Structural Geology, 141: 104209. https://doi.org/10.1016/j.jsg.2020.104209

[14] Carriere, S., Chalikakis, K., Danquigny, C., Sénéchal, Chapelet, A. (2012). Complementarity of electrical resistivity tomography and ground penetrating radar to study karst unsaturated zone. Journal of Applied Geophysics, 94(4): 31-41. https://doi.org/10.1016/j.jappgeo.2013.03.014

[15] Sibul, I., Plado, J., Jõeleht, A. (2017). Ground-penetrating radar and electrical resistivity tomography for mapping bedrock topography and fracture zones: a case study in Viru-Nigula, NE Estonia. Estonian Journal of Earth Sciences, 66(3): 142. https://doi.org/10.3176/earth.2017.11

[16] Drahor, M.G. (2019). Identification of gypsum karstification using an electrical resistivity tomography technique: the case-study of the Sivas gypsum karst area (Turkey). Engineering Geology, 252: 78-98. https://doi.org/10.1016/j.enggeo.2019.02.019

[17] Xue, Y., Kong, F., Li, S., Qiu, D., Su, M., Li, Z., Zhou, B. (2021). Water and mud inrush hazard in underground engineering: Genesis, evolution and prevention. Tunnelling and Underground Space Technology, 114:

103987. https://doi.org/10.1016/j.tust.2021.103987

[18] Zhao, J., Liu, W., Shen, J., Xu, M., Sasmito, A.P. (2022). A real-time monitoring temperature-dependent risk index for predicting mine water inrush from collapse columns through a coupled thermal–hydraulic-mechanical model. Journal of Hydrology, 607: 127565. https://doi.org/10.1016/j.jhydrol.2022.127565

[19] Wang, J., Li, S., Li, L., Shi, S., Zhou, Z., Song, S. (2020). Mechanism of water inrush in fractures and block collapse under hydraulic pressure. Mathematics and Computers in Simulation, 177: 625-642. https://doi.org/10.1016/j.matcom.2020.05.028

[20] Huang, L., Ma, J., Lei, M., Liu, L., Lin, Y., Zhang, Z. (2020). Soil-water inrush induced shield tunnel lining damage and its stabilization: a case study. Tunnelling and Underground Space Technology, 97: 103290. https://doi.org/10.1016/j.tust.2020.103290